

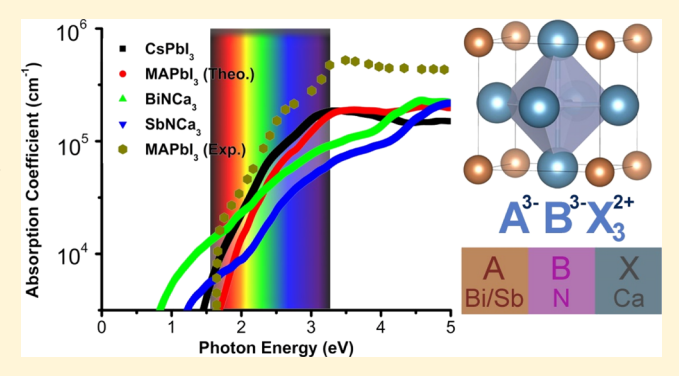
Bi(Sb)NCa₃: Expansion of Perovskite Photovoltaics into All-Inorganic **Anti-Perovskite Materials**

Jun Dai, ** Ming-Gang Ju, ** Liang Ma, ** and Xiao Cheng Zeng*, **, ** and Xiao Cheng Zeng*, **, **

[†]Department of Chemistry and [‡]Department of Mechanical and Materials Engineering, University of Nebraska-Lincoln, Lincoln, Nebraska 68588, United States

Supporting Information

ABSTRACT: Perovskite photovoltaics (PVs) have attracted intense interest largely because of their high power conversion efficiency and low cost. The chemical structures of perovskite materials can be generally described by the formula of ABX₃, where cations occupy "A" and "B" sites and anions occupy "X" sites. Herein, we present a comprehensive theoretical study of two inorganic anti-perovskite materials, namely, BiNCa3 and SbNCa₃, for perovskite PVs. Note that in anti-perovskites, anions occupy "A" and "B" sites, whereas cations occupy "X" sites. Specifically, for both materials, we investigate their thermodynamic stability, dynamic stability, optoelectronic properties and defect properties through ab initio calculations. Our computation suggests that both BiNCa₃ and SbNCa₃



possess direct band gaps of 0.65 and 1.14 eV, respectively. Notably, both materials are predicted to be thermodynamically stable, as demonstrated by their relatively large stable region based on the phase stability analysis. Dynamic and thermal stabilities are also suggested via the computed phonon spectra and ab initio molecular dynamics simulation. Furthermore, both materials possess desired optical absorption coefficients in the visible light region, comparable to that of the prevailing organic inorganic hybrid perovskite, MAPbI3. Both exhibit enhanced optical absorption in the infrared region and have good defect tolerance. Lastly, good n-type and p-type conductivity may be realized by controlling the growth condition. The combined desirable properties render both BiNCa₃ and SbNCa₃ as promising all-inorganic and lead-free optical absorbers for PV application.

■ INTRODUCTION

Owing to their extraordinary optoelectronic properties, for example, low-temperature solution processability, 1,2 large absorption coefficient,³ high carrier mobility,⁴ long diffusion length, 5-8 and unique defect-tolerant feature, 9-12 organicinorganic hybrid perovskite (OIHP) materials have been widely viewed as highly promising absorber materials for solar cells. 3,13-15 Remarkably, fast increase of the power conversion efficiency (PCE) for OIHP solar cells has been witnessed over just few years. 16 The highest PCE value (~23.7%) of OIHP solar cells is already comparable to the PCE value of commercial silicon-based solar cells. Although considerable progress has been made in the research of thin-film solar cells based on CH₃NH₃PbI₃ (MAPbI₃), their commercialization is still hampered by some obstacles, such as the inherent structural instability because of easy degradation upon exposure to water, oxygen, illumination, and high temperature. Moreover, the toxicity of the water-soluble Pb²⁺ ion is also a concern. 17,18

Halide perovskite materials generally possess a formula of ABX_3 (A = MA⁺, FA⁺, Cs⁺; B = Pb²⁺; X = Cl⁻, Br⁻, I⁻). It has been reported that partial replacement of MA+ or FA+ with an inorganic element Cs+ can greatly enhance the stability of

OIHP. On the other hand, a great deal of effort has been made to the exploration of lead-free perovskites by replacing the B site Pb^{2+,18-20} Divalent (Ge²⁺ and Sn²⁺), ²¹⁻²⁴ trivalent (Sb³⁺ and Bi^{3+}), 25,26 and tetravalent (Ge^{4+} , Sn^{4+} , and Ti^{4+}) ${}^{27-29}$ all have been explored as lead replacement. Among these materials, neither Ge²⁺ nor Sn²⁺ is in its stable oxidization state, which limits their utilization for photovoltaic (PV) applications. Meanwhile, the trivalent replacements based on Sb and Bi tend to yield a band gap larger than 2.0 eV, which is unsuitable for PVs. Although the tetravalent Cs₂SnI₆ shows good stability in open-air and moisture environment, the presence of dominant I vacancy and Sn interstitial defects as well as the low carrier mobility is undesirable for PV applications.²⁷ Recently, growing interest has been paid to elpasolite or ordered double perovskite where the B site cation (Pb^{2+}) is replaced by monovalent B' (Cu^+, Ag^+, Au^+) and trivalent B" $(Bi^{3+}, Sb^{3+}, In^{3+}, Ga^{3+})$ metal ions. $^{30-43}$ Although first-principles calculations predicted a number of related materials with promising electronic and optical properties, 30,31

Received: December 7, 2018 Revised: February 16, 2019 Published: February 26, 2019

investigation of these double perovskites for PV applications is still lacking. In particular, synthesized $Cs_2AgBiCl_6$ and $Cs_2AgBiBr_6$ show a wide indirect band gap and large effective carrier masses. ^{35,37,43,44} Although MA₂TlBiBr₆ displays promising properties, Tl is still a strongly toxic element. ⁴² Hence, more research work is needed to assess the full potential of this class of materials.

In addition to the conventional perovskite ABX₃, where cations occupy the A and B sites with anions occupying the X sites, there also exists a class of antiperovskite materials in which anions occupy the A and B sites, whereas cations occupy the X sites. 45 Like the conventional perovskites, anti-perovskites can also display a wide variety of novel properties, including thermoelectric, 46 giant magnetoresistance, 47 superconducting, 48 etc., owing to their composition flexibility to accommodate diverse anions (at A and B sites) and cations (at X sites). Recently, anti-perovskite materials have also been predicted to be promising superionic conductors, 49,50 as in the case of some traditional organic-inorganic halide perovskites with high ionic conductivity. 51 The structure and composition diversities of anti-perovskites provide another promising platform for the exploration of lead-free absorber materials. Gebhardt and Rappe have theoretically studied several organic-inorganic hybrid anti-perovskite materials and transition-metal hybrid anti-perovskites. 52,53 The structural uncertainty introduced by the volatile MA+/FA+ group, however, requires further investigation in future experiments. All inorganic anti-perovskite structures appear to be more predictable than the hybrid ones, a good starting point for the exploration. Note that more than 2 decades ago, a series of MNCa₃ (M=P, As, Sb, Bi, Ge, Sn and Pb) have been successfully synthesized.⁴⁵ Previous computation at the modified Becke-Johnson level also predicted direct band gaps of 1.1 and 1.09 eV for SbNCa₃ and BiNCa₃, respectively, which are within optimal band gap values for solar absorbers. Besides good optical absorption, a promising absorber material should also be highly stable with good defect tolerance. It will be interesting to see whether these lead-free materials can be good solar absorber materials for optoelectronic applications.

In this work, we investigate various relevant properties of BiNCa₃ and SbNCa₃ as potential optical absorbers, for example, the electronic, optical and defect properties, as well as dynamic and thermodynamic stabilities. Both BiNCa₃ and SbNCa₃ are predicted to possess a direct band gap of 0.65 and 1.14 eV, respectively. Phonon spectrum calculations suggest their dynamic stability, while a wide thermodynamically stable range for equilibrium growth is also predicted for BiNCa₃ and SbNCa₃. Optical absorption is as good as that of the prevailing MAPbI₃ perovskite. Last but not least, both materials exhibit good defect tolerance and flexible conductivity, from good n-type to good p-type, depending on the growth condition.

■ COMPUTATIONAL DETAILS

All calculations were performed within the framework of density functional theory as implemented in the Vienna Ab initio Simulation Package (VASP 5.4). The generalized gradient approximation in the form of Perdew–Burke–Ernzerhof (PBE) functional and projector augmented wave potentials were used. Both BiNCa₃ and SbNCa₃ have been found to be in cubic structure with space group ($Pm\overline{3}m$), where Sb/Bi occupies the corner positions in Wyckoff position 1b (0.5, 0.5, 0.5), N is at the center position in 1a (0, 0, 0), and Ca is at the face center position in 3c (0, 0.5, 0.5), as shown in

Figure 1. The optimized lattice constants of BiNCa₃ and SbNCa₃ are 4.92 and 4.87 Å, respectively, about 0.6% and 0.4%

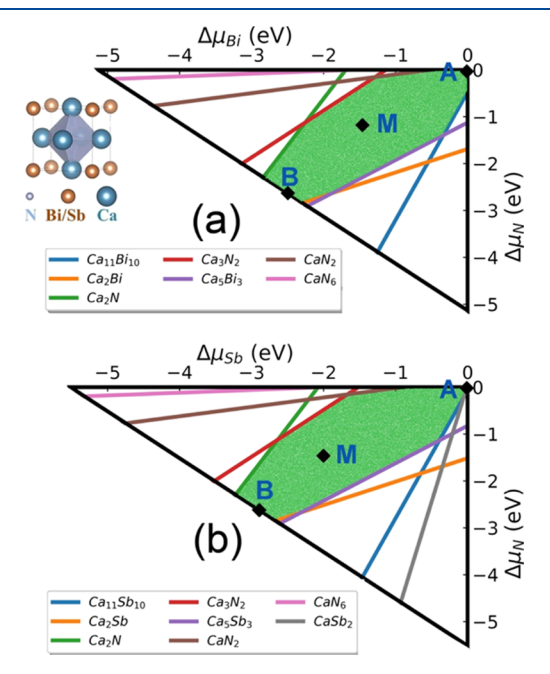


Figure 1. Thermodynamic stable region for equilibrium growth of (a) BiNCa₃ and (b) SbNCa₃, as marked by green color. A, B, and M are three representative points chosen for the formation energy calculations, where for BiNCa₃ (A: $\Delta\mu_{\rm Bi}=\Delta\mu_{\rm N}=0$ eV, $\Delta\mu_{\rm Ca}=-1.71$ eV; M: $\Delta\mu_{\rm Bi}=-1.50$ eV, $\Delta\mu_{\rm N}=-1.20$ eV, $\Delta\mu_{\rm Ca}=-0.81$ eV; B: $\Delta\mu_{\rm Bi}=-2.50$ eV, $\Delta\mu_{\rm N}=-2.63$ eV, $\Delta\mu_{\rm Ca}=0$ eV) and for SbNCa₃ (A: $\Delta\mu_{\rm Sb}=\Delta\mu_{\rm N}=0$ eV, $\Delta\mu_{\rm Ca}=-1.84$ eV; M: $\Delta\mu_{\rm Sb}=-2.0$ eV, $\Delta\mu_{\rm N}=-1.5$ eV, $\Delta\mu_{\rm Ca}=-0.54$ eV; B: $\Delta\mu_{\rm Sb}=-2.9$ eV, $\Delta\mu_{\rm N}=-2.62$ eV, $\Delta\mu_{\rm Ca}=0$ eV). The inset at top left is the structure model of BiNCa₃ or SbNCa₃.

larger than the experimental values. 45 This result indicates that the PBE functional can accurately describe the structural properties of BiNCa₃ and SbNCa₃. An energy cutoff of 450 eV was adopted for the plane wave expansion of the electronic wave function. Geometric structures were relaxed until the force on each atom was less than 0.01 eV/Å while the energy convergence criteria of 1×10^{-5} eV were adopted. For the electronic structure calculations, both PBE functional and hybrid HSE06 functional (with value of $\alpha = 0.2$)⁵⁷ with and without spin-orbit coupling (SOC) were examined. The inclusion of SOC is to accurately describe the strong relativistic features of heavy element Bi in the compounds. The primitive unit cell and a Γ -centered $9 \times 9 \times 9$ *k*-mesh were used. For the band structure calculation, high-symmetry points R (0.5, 0.5, 0.5), X (0.0, 0.5, 0.0), Γ (0.0, 0.0, 0.0), and M (0.5, 0.5, 0.0) were considered. For each path along R-X, $X-\Gamma$ and $\Gamma-M$, 20 k-points were used. For defect energy calculations, the supercell with 320 atoms and the Γ -only k-mesh were used. Atomic positions of the defect structures were relaxed until the force on each atom was less than 0.02 eV/Å. For a defect D in a charge state of q, the defect formation energy (DFE) was calculated via the formula

DFE(D^q) =
$$E_{D^q} - E_H - \sum_i n_i \mu_i + q(E_F + E_V)$$

+ E^q (corr)

where E_{D^q} and E_H are the total energies of the supercell in charge state q and the defect-free host supercell, respectively. $E_{\rm F}$ is the Fermi level (a variable for computations shown in Figure 4) with respect to the valence band maximum of the defect-free host supercell, E_v . n_i is the number atoms of type i added (>0) or removed (<0) in the supercell as compared to the host supercell. μ_i is the chemical potential of the type i atom, which can be calculated with respect to its elemental phase (i.e., the chemical potential of the most stable elemental phase of type i, μ_{el}) by $\mu_i = \mu_{el} + \Delta \mu_i$. Note that $\Delta \mu_i$ depends on the chemical condition, e.g., point A, B, and M shown in Figure 1 (see Supporting Information for details). $E^q(\text{corr})$ is a correction term to the electrostatic potential in the perfect bulk and defect supercells, which is to account for the finite size effects on the total energies of charged defects.⁵⁸ calculated dielectric constants of 29.57 for BiNCa₃ and 27.48 for SbNCa3 were used to assess the correction. The optical absorption coefficient can be computed based on the real $[\varepsilon_1(\omega)]$ and imaginary $[\varepsilon_2(\omega)]$ part of the frequencydependent dielectric function $[\varepsilon(\omega)]$, where the imaginary part is determined by a summation over empty states, whereas the real part is determined by the usual Kramers-Kronig transformation.⁵⁹ For this computation, the number of bands was set to be 5 times of the default number. The absorption coefficient i s given $\alpha(\omega) = \frac{\sqrt{2}E}{\hbar} [\sqrt{\varepsilon_1^2(\omega) + \varepsilon_2^2(\omega)} - \varepsilon_1(\omega)]^{1/2}$, where E represents phonon energy and ħ represents reduced Planck's constant.

RESULTS AND DISCUSSION

Stability. For the synthesis of BiNCa₃ and SbNCa₃, the starting precursors are usually a mixture of elemental (Bi, Sb, Ca, and N₂) or binary phases (Ca₃N₂, CaN₂, Ca₂Bi, Ca₂Sb, etc.). For example, Bi or Sb and Ca₃N₂ have been used to synthesize BiNCa₃ and SbNCa₃. From thermodynamic point of view, whether BiNCa₃ or SbNCa₃ can be synthesized or not is dependent on the competition of the formation energies. To address the thermodynamic stability of BiNCa₃ and SbNCa₃, we performed phase stability analysis by taking into account the decomposition channels into various combinations of competing phases, including all existing compounds.³¹ The stable region, a polygon as marked in green, is plotted in Figure 1a, using $\Delta \mu_{\rm Bi}$ and $\Delta \mu_{\rm N}$ as variables ($\Delta \mu_{\rm Ca}$ is dependent on them), where BiNCa₃ can be synthesized without the coexistence of the elementary or secondary phases. In general, the narrower the stable region is, the more important the composition control is for the synthesis of single-phase samples. Compared to In- or Ga-based double perovskites, 31,39 CuSbS₃⁶⁰ or Cu₂ZnSnS₄,⁶¹ we can see a larger stable region, implying that BiNCa₃ can be relatively easy to synthesize through controlling the Bi and N contents. By applying the same procedures to SbNCa₃, we find that SbNCa₃ can also be stabilized within a relatively large region, as shown in Figure

Thermal stability of BiNCa₃ and SbNCa₃ was examined by using the Born–Oppenheimer molecular dynamics (BOMD) in the constant temperature and constant pressure ensemble (*NpT*). The temperature (338 K, 65 °C) and pressure (0 Pa) were controlled by the Parrinello–Rahman method combined with a Langevin thermostat. A temperature of 338 K was kept during the BOMD simulation since it is a commonly used temperature for solar cell stability test. The time step for

BOMD was set to 1 fs, and each BOMD simulation lasted 10 ps, following previous simulation studies. ^{64,65} As shown in Figure S1, after 10 ps of BOMD simulation, both BiNCa₃ and SbNCa₃ show slight structural changes, suggesting their good structural integrity. Lastly, the phonon spectra of both materials, as shown in Figure S2, were computed. No imaginary phonon frequencies exist for both materials, reflecting their dynamic stability. Overall, these combined calculations and simulation suggest that BiNCa₃ and SbNCa₃ are indeed thermodynamically stable, a notion supported by the experimental fact that both have already been synthesized. ⁴⁵

Electronic Structure. For both BiNCa₃ and SbNCa₃, we computed their band structures and atomic- and orbital-projected density of states (DOS) at HSE06 level with SOC (see Figure 2). We can see that both the valence band

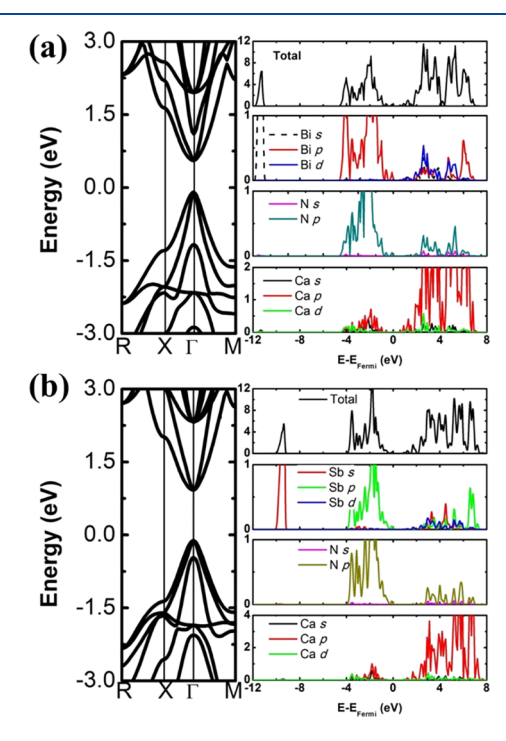


Figure 2. HSE06 + SOC band structure, and total and projected DOS for (a) BiNCa₃ and (b) SbNCa₃. R (0.5, 0.5, 0.5), X (0.0, 0.5, 0.0), Γ (0.0, 0.0, 0.0), and M (0.5, 0.5, 0.0) denote high-symmetry points.

maximum (VBM) and conduction band minimum (CBM) are located at Γ , giving a direct band gap. As illustrated in the atomic- and orbital-projected DOS (see Figure 2), the VBM is contributed by the p states of Bi/Sb and N sites, whereas the CBM is mostly composed of the d states of Ca, and partially of the d states of Bi/Sb. HSE06 results without considering SOC were also obtained for the purpose of comparison (see Figure S3). Specifically, HSE06 predicted band gaps of 1.06 and 1.16 eV, whereas HSE06 + SOC gave 0.65 and 1.14 eV for BiNCa₃ and SbNCa₃, respectively. Inclusion of SOC has a significant effect on the computed band structure of BiNCa₃, reducing the band gap from 1.06 eV in HSE06 to 0.65 eV in HSE06 + SOC. The SOC has a strong impact on the p states of VBM, where the three-fold degenerated bands at Γ are split, with SOC being included, and the energy difference of the split p states is 1.06 and 0.36 eV for BiNCa₃ and SbNCa₃, respectively.

The effective masses of electron and hole were calculated using the finite-difference code developed by Fonari and

Sutton, where the second derivatives were evaluated on the five-point stencil. 66 As VBM shows double degeneracy at Γ point for BiNCa₃ and SbNCa₃, the effective mass of hole splits into light and heavy ones, denoted as m_h^* (light hole) and m_{hh}^* (heavy hole). For electrons, as CBM also shows double degeneracy, we calculated the effective mass from the second lowest conduction band, namely, m_e^* and $m_{e,2}^*$. For both materials, the anisotropies of the computed m_{lh}^* , m_{hh}^* , m_e^* , and $m_{\rm e,2}^*$ are negligible (see Table S1). As summarized in Table 1,

Table 1. Computed Band Gap (E_g) , Effective Masses of Electrons, or Effective Masses of Light and Heavy Holes of BiNCa₃ and SbNCa₃^a

	$E_{ m g}$	$m_{ m lh}^*$	$m_{ m hh}^*$	$m_{\rm e}^*$	$m_{\mathrm{e,2}}^*$
BiNCa ₃	0.65	0.07	0.37	0.10	0.82
$SbNCa_3$	1.14	0.13	0.43	0.13	0.82

^aThe effective masses are in units of the rest mass of an electron m_a .

the calculated m_{hh}^* and $m_{e,2}^*$ for BiNCa₃ are $0.37m_e$ and $0.82m_e$, whereas for SbNCa₃, they are $0.43m_e$ and $0.82m_e$, respectively. The electron from the second lowest conduction band and the heavy hole have higher DOS, compared to the light ones, which tend to dominate the transport properties at shorter diffusion length, whereas at longer diffusion distances, the light hole and electron from the lowest conduction band will start to dominate the transport because of their longer diffusion length. The computed m_{lh}^* and m_e^* for both materials are around $0.1m_e$. Note that the electron and hole effective masses of the prototype MAPbI₃ are $\sim 0.1-0.2m_e$. Although the charge carrier mobility at working condition is highly complicated (related to scattering probability, temperature, etc.), the relatively low effective masses for both materials suggest good transport properties.

Defect Properties. It is well-known that the defect properties of the optical absorbers are very important to the performance of PV application. 9,10,12,69 Here, we calculated the formation energies of 12 intrinsic point defects for BiNCa₃ and SbNCa₃, including three vacancies (V_M, V_N, and V_{Ca}), three interstitials (M_i, N_i, and Ca_i), and six antisites (M_N, M_{Ca}, Ca_M, Ca_N, N_M, and N_{Ca}), where M stands for Bi or Sb. The formation energies depend on the chemical potentials of the related elements. Generally, the higher the chemical potential is for a given element, the richer the environment is for this element. Here, three representative chemical conditions in the stable region (where the single phase of BiNCa₃ or SbNCa₃ can be synthesized) are chosen, namely, (A) Bi(Sb) rich, N rich, and Ca lean; (B) Bi(Sb) lean, N lean, and Ca rich; and (M) medium condition as marked in Figure 1. Detailed results of chemical potentials at (A), (B), and (M) can be found in the figure caption. The calculated formation energies of possible neutral point defects are plotted in Figure 3. Under Bi, N-rich, Ca lean condition, the acceptor defect V_{Ca} (Ca vacancy) has the lowest formation energy (1.29 eV), followed by Bi_{Ca} (1.33 eV), another acceptor defect. Under the medium condition, the donor defects $V_{\rm N}$ are dominant with the lowest formation energy of 1.36 eV. Under Bi, N lean, Ca-rich condition, the formation energy of V_N becomes slightly negative (-0.08 eV), indicating that an unusually high concentration of N vacancies may exist under this condition. The system may even lower its energy by undergoing transition to another state with an ordered arrangement of these N vacancies.

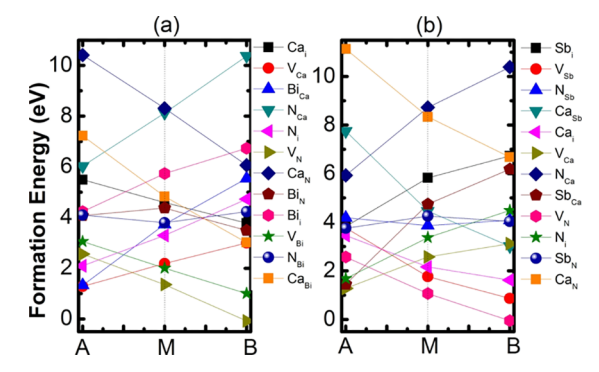


Figure 3. Formation energies (DFEs) of neutral intrinsic point defects in BiNCa₃ and SbNCa₃ at chemical potentials A, B, and M (see Figure

In Figure 4, we plot the formation energies of the 12 intrinsic point defects when they are ionized at different charge states under Bi(Sb), N-rich, Ca lean condition and medium condition; Bi(Sb), N lean condition is not discussed because under this condition, the concentration of N vacancy might be too high for applications. As formulated above, the formation energy depends on the Fermi level of the samples. For example, the formation energy of charged acceptors decreases with the increase of Fermi energy from VBM to CBM. The turning points in Figure 4 for different defects under different conditions correspond to their transition energy level. For BiNCa₃, under Bi, N-rich condition, the (-1/-2) charge state (q) transition level of the dominant V_{Ca} acceptor is shallow, lies at 0.07 eV above the VBM (blue dot in Figure 4a), indicating that the V_{Ca} defect can be easily ionized at room temperature. The ionization of V_{Ca} defect produces one hole carrier. Another acceptor defect Bi_{C2} does not has transition level within the band gap. These results hint that under Bi, Nrich condition, BiNCa₃ could be intrinsically a good p-type semiconductor. Although under medium condition the donor defects V_N are the dominant ones, their (0/1+) charge state transition level is also quite shallow, lies at 0.01 eV below the CBM (lower dot in Figure 4b), which could be a good source for n-type conductivity. The (0/2+) level of the other donor defect V_{Bi} is also very shallow, lies at 0.03 eV below the CBM. These properties show that under medium condition, BiNCa₃ could be a good n-type semiconductor. Thus, it would be possible to realize either good n-type or good p-type conductivity in BiNCa₃ by controlling the synthesis condition. For SbNCa₃, its defect properties are quite similar to those of BiNCa₃, whose dominating acceptor V_{Ca} has a $\left(-1/-2\right)$ charge state transition level lying at 0.1 eV above the VBM under Sb, N-rich condition and dominating donor V_N has a (0/1+) level at 0.01 eV below the CBM under medium condition (Figure 4c,d). For both BiNCa₃ and SbNCa₃, the dominating defects with low energies have shallow levels, so that they could be considered as good solar absorber materials free of recombination center defects.

To examine if BiNCa₃ and SbNCa₃ can be good solar absorbers, we first checked their values of the open-circuit voltage (V_{OC}) and PCE (η) under the Shockley-Queisser limit for single-junction solar cells. The predicted $V_{\rm OC}$ and η values under the Shockley-Queisser limit for direct band gap semiconductors with gaps of 0.65 eV and 1.14 V are 0.52 V, 23.9%, and 0.88 V and 32.4%, respectively.⁷⁰ The computed absorption coefficients of BiNCa₃ and SbNCa₃ are plotted in Figure 5, with no experimental absorption data available. We

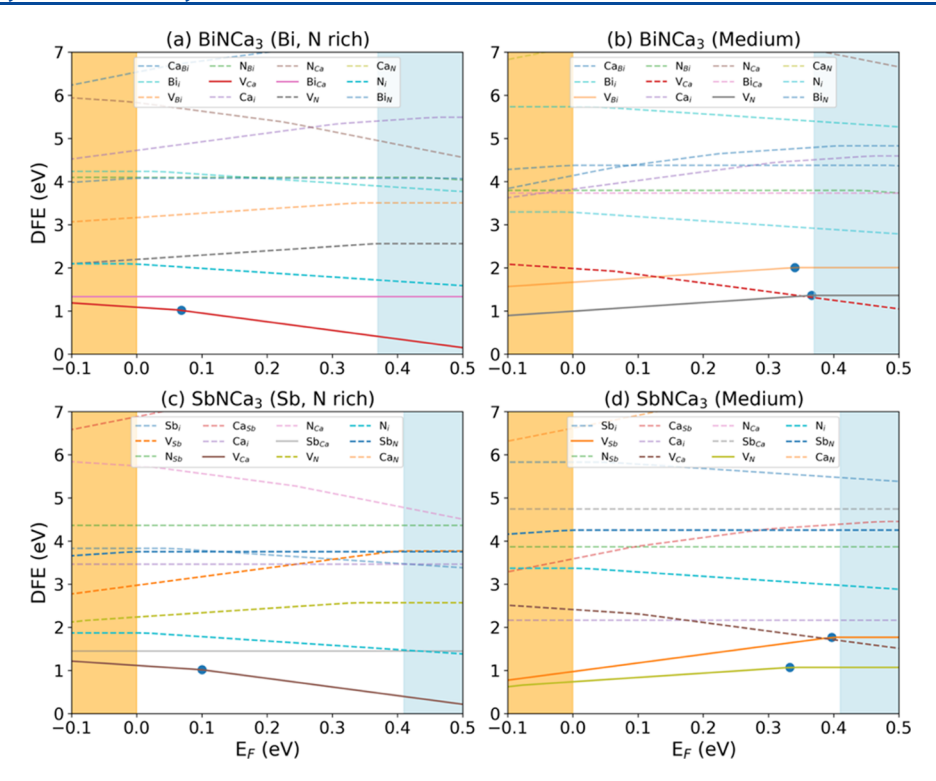


Figure 4. Formation energies (DFEs) of intrinsic point defects in BiNCa₃ and SbNCa₃ at chemical potentials A [Bi(Sb), N rich] and M (medium condition), as shown in Figure 1. Defects with high DFEs are shown in dashed lines. Blue dots at the bent point of two straight lines refer to the charge-state transition. The value of E_F is varied from valence band maximum to conduction band minimum.

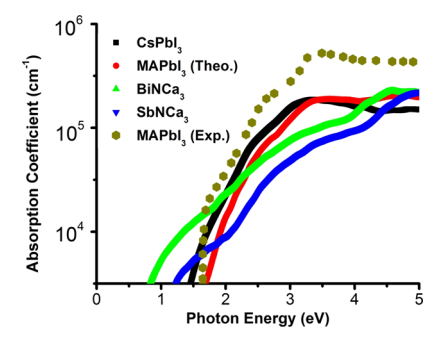


Figure 5. Computed optical absorption spectra of BiNCa₃ and SbNCa₃, CsPbI₃. Theoretical and experimental spectra of MAPbI₃ are also plotted for the purpose of comparison. The experimental absorption spectrum of MAPbI₃ is taken from ref 71.

calculated and plotted those from MAPbI3 and CsPbI3 at the same level for comparison, and the experimental absorption of MAPbI₃ was also plotted. Here, a photon energy range of 0-4 eV is used, which covers the photon energy in solar spectrum. Benefitted from the p-d transition from VBM to CBM, the overall absorption coefficients of BiNCa₃ and SbNCa₃ in the visible light region are comparable to those of MAPbI₃ and CsPbI₃. Specifically, owing to the smaller band gap compared to MAPbI₃, BiNCa₃ and SbNCa₃ show good absorption in the infrared region, indicating that they might be good alternatives as the narrow band gap material in tandem solar cells.

CONCLUSIONS

In conclusion, we have investigated optoelectronic and defect properties of two all-inorganic anti-perovskites, BiNCa₃ and SbNCa₃, by using first-principles calculations. On the basis of computation results, we find that both materials possess direct band gaps (0.65 and 1.14 eV), relatively small effective mass of charge carriers, good optical absorption comparable to MAPbI₃, and good defect tolerance. The computed formation energies show that both materials are thermodynamically stable against decomposition, while phonon spectrum calculation also shows that both materials are dynamically stable. These desired properties, including modest band gaps and good absorption in the infrared region, suggest that BiNCa₃ and SbNCa₃ are potentially good solar absorber materials, and both can be employed as a narrow band gap absorber material in tandem solar cells.

ASSOCIATED CONTENT

S Supporting Information

The Supporting Information is available free of charge on the ACS Publications website at DOI: 10.1021/acs.jpcc.8b11821.

Phase stability analysis, snapshots of ab initio MD simulations with temperature being controlled at 338 K (65 °C), computed HSE06 band structures without SOC, computed phonon DOS, and effective masses of electrons, light and heavy holes along three normal directions for BiNCa₃ and SbNCa₃ (PDF)

AUTHOR INFORMATION

Corresponding Author

*E-mail: xzeng1@unl.edu.

ORCID ®

Jun Dai: 0000-0001-6599-8826 Ming-Gang Ju: 0000-0003-4285-7937 Liang Ma: 0000-0003-4747-613X

Xiao Cheng Zeng: 0000-0003-4672-8585

Notes

The authors declare no competing financial interest.

ACKNOWLEDGMENTS

The project is supported by the National Science Foundation (NSF) through the Nebraska Materials Research Science and Engineering Center (MRSEC) (grant no. DMR-1420645), an NSF EPSCoR Track-2 grant (OIA-1538893), and by the University of Nebraska Holland Computing Center.

REFERENCES

- (1) Burschka, J.; Pellet, N.; Moon, S.-J.; Humphry-Baker, R.; Gao, P.; Nazeeruddin, M. K.; Grätzel, M. Sequential Deposition as a Route to High-Performance Perovskite-Sensitized Solar Cells. *Nature* **2013**, 499, 316–319.
- (2) Yang, M.; Li, Z.; Reese, M. O.; Reid, O. G.; Kim, D. H.; Siol, S.; Klein, T. R.; Yan, Y.; Berry, J. J.; van Hest, M. F. A. M.; Zhu, K. Perovskite Ink with Wide Processing Window for Scalable High-Efficiency Solar Cells. *Nat. Energy* **2017**, *2*, 17038.
- (3) Green, M. A.; Ho-Baillie, A.; Snaith, H. J. The Emergence of Perovskite Solar Cells. *Nat. Photonics* **2014**, *8*, 506–514.
- (4) Wehrenfennig, C.; Eperon, G. E.; Johnston, M. B.; Snaith, H. J.; Herz, L. M. High Charge Carrier Mobilities and Lifetimes in Organolead Trihalide Perovskites. *Adv. Mater.* **2013**, *26*, 1584–1589.
- (\hat{S}) Dong, Q.; Fang, Y.; Shao, Y.; Mulligan, P.; Qiu, J.; Cao, L.; Huang, J. Electron-hole diffusion lengths > 175 μ m in solution-grown CH₃NH₃PbI₃ single crystals. *Science* **2015**, 347, 967–970.
- (6) Shi, D.; Adinolfi, V.; Comin, R.; Yuan, M.; Alarousu, E.; Buin, A.; Chen, Y.; Hoogland, S.; Rothenberger, A.; Katsiev, K.; Losovyj, Y.; Zhang, X.; Dowben, P. A.; Mohammed, O. F.; Sargent, E. H.; Bakr, O. M. Low Trap-State Density and Long Carrier Diffusion in Organolead Trihalide Perovskite Single Crystals. *Science* 2015, 347, 519–522.
- (7) Stranks, S. D.; Eperon, G. E.; Grancini, G.; Menelaou, C.; Alcocer, M. J. P.; Leijtens, T.; Herz, L. M.; Petrozza, A.; Snaith, H. J. Electron-Hole Diffusion Lengths Exceeding 1 Micrometer in an Organometal Trihalide Perovskite Absorber. *Science* **2013**, 342, 341–344.
- (8) Zhao, D.; Yu, Y.; Wang, C.; Liao, W.; Shrestha, N.; Grice, C. R.; Cimaroli, A. J.; Guan, L.; Ellingson, R. J.; Zhu, K. Low-Bandgap Mixed Tin—Lead Iodide Perovskite Absorbers with Long Carrier Lifetimes for All-Perovskite Tandem Solar Cells. *Nat. Energy* **2017**, *2*, 17018.
- (9) Yin, W.-J.; Shi, T.; Yan, Y. Unique Properties of Halide Perovskites as Possible Origins of the Superior Solar Cell Performance. *Adv. Mater.* **2014**, *26*, 4653–4658.
- (10) Yin, W.-J.; Shi, T.; Yan, Y. Unusual Defect Physics in Ch₃NH₃PbI₃ Perovskite Solar Cell Absorber. *Appl. Phys. Lett.* **2014**, *104*, 063903.
- (11) Yin, W.-J.; Yang, J.-H.; Kang, J.; Yan, Y.; Wei, S.-H. Halide Perovskite Materials for Solar Cells: A Theoretical Review. *J. Mater. Chem. A* **2015**, *3*, 8926–8942.
- (12) Huang, J.; Yuan, Y.; Shao, Y.; Yan, Y. Understanding the Physical Properties of Hybrid Perovskites for Photovoltaic Applications. *Nat. Rev. Mater.* **2017**, *2*, 17042.
- (13) Snaith, H. J. Perovskites: The Emergence of a New Era for Low-Cost, High-Efficiency Solar Cells. *J. Phys. Chem. Lett.* **2013**, *4*, 3623–3630.
- (14) Green, M. A.; Ho-Baillie, A. Perovskite Solar Cells: The Birth of a New Era in Photovoltaics. ACS Energy Lett. 2017, 2, 822–830.
- (15) Petrus, M. L.; Schlipf, J.; Li, C.; Gujar, T. P.; Giesbrecht, N.; Müller-Buschbaum, P.; Thelakkat, M.; Bein, T.; Hüttner, S.; Docampo, P. Capturing the Sun: A Review of the Challenges and Perspectives of Perovskite Solar Cells. *Adv. Energy Mater.* **2017**, *7*, 17002.64.
- (16) Yang, W. S.; Park, B.-W.; Jung, E. H.; Jeon, N. J.; Kim, Y. C.; Lee, D. U.; Shin, S. S.; Seo, J.; Kim, E. K.; Noh, J. H.; Seok, S. I. Iodide management in formamidinium-lead-halide-based perovskite layers for efficient solar cells. *Science* **2017**, *356*, 1376–1379.

- (17) Grätzel, M. The Light and Shade of Perovskite Solar Cells. *Nat. Mater.* **2014**, *13*, 838–842.
- (18) Abate, A. Perovskite Solar Cells Go Lead Free. *Joule* 2017, 1, 659-664.
- (19) Kamat, P. V.; Bisquert, J.; Buriak, J. Lead-Free Perovskite Solar Cells. ACS Energy Lett. 2017, 2, 904–905.
- (20) Chakraborty, S.; Xie, W.; Mathews, N.; Sherburne, M.; Ahuja, R.; Asta, M.; Mhaisalkar, S. G. Rational Design: A High-Throughput Computational Screening and Experimental Validation Methodology for Lead-Free and Emergent Hybrid Perovskites. *ACS Energy Lett.* **2017**, *2*, 837–845.
- (21) Ju, M.-G.; Dai, J.; Ma, L.; Zeng, X. C. Lead-Free Mixed Tin and Germanium Perovskites for Photovoltaic Application. *J. Am. Chem. Soc.* **2017**, *139*, 8038–8043.
- (22) Hao, F.; Stoumpos, C. C.; Cao, D. H.; Chang, R. P. H.; Kanatzidis, M. G. Lead-Free Solid-State Organic-Inorganic Halide Perovskite Solar Cells. *Nat. Photonics* **2014**, *8*, 489–494.
- (23) Noel, N. K.; Stranks, S. D.; Abate, A.; Wehrenfennig, C.; Guarnera, S.; Haghighirad, A.-A.; Sadhanala, A.; Eperon, G. E.; Pathak, S. K.; Johnston, M. B.; Petrozza, A.; Herz, L. M.; Snaith, H. J. Lead-free organic—inorganic tin halide perovskites for photovoltaic applications. *Energy Environ. Sci.* **2014**, *7*, 3061—3068.
- (24) Stoumpos, C. C.; Frazer, L.; Clark, D. J.; Kim, Y. S.; Rhim, S. H.; Freeman, A. J.; Ketterson, J. B.; Jang, J. I.; Kanatzidis, M. G. Hybrid Germanium Iodide Perovskite Semiconductors: Active Lone Pairs, Structural Distortions, Direct and Indirect Energy Gaps, and Strong Nonlinear Optical Properties. J. Am. Chem. Soc. 2015, 137, 6804–6819.
- (25) Saparov, B.; Hong, F.; Sun, J.-P.; Duan, H.-S.; Meng, W.; Cameron, S.; Hill, I. G.; Yan, Y.; Mitzi, D. B. Thin-Film Preparation and Characterization of Cs3sb2i9: A Lead-Free Layered Perovskite Semiconductor. *Chem. Mater.* **2015**, 27, 5622–5632.
- (26) Park, B.-W.; Philippe, B.; Zhang, X.; Rensmo, H.; Boschloo, G.; Johansson, E. M. J. Bismuth Based Hybrid Perovskites $A_3Bi_2I_9$ (A: Methylammonium or Cesium) for Solar Cell Application. *Adv. Mater.* **2015**, *27*, 6806–6813.
- (27) Saparov, B.; Sun, J.-P.; Meng, W.; Xiao, Z.; Duan, H.-S.; Gunawan, O.; Shin, D.; Hill, I. G.; Yan, Y.; Mitzi, D. B. Thin-Film Deposition and Characterization of a Sn-Deficient Perovskite Derivative Cs₂SnI₆. *Chem. Mater.* **2016**, *28*, 2315–2322.
- (28) Lee, B.; Stoumpos, C. C.; Zhou, N.; Hao, F.; Malliakas, C.; Yeh, C.-Y.; Marks, T. J.; Kanatzidis, M. G.; Chang, R. P. H. Air-Stable Molecular Semiconducting Iodosalts for Solar Cell Applications: Cs₂SnI₆ as a Hole Conductor. *J. Am. Chem. Soc.* **2014**, *136*, 15379–15385.
- (29) Ju, M.-G.; Chen, M.; Zhou, Y.; Garces, H. F.; Dai, J.; Ma, L.; Padture, N. P.; Zeng, X. C. Earth-Abundant Nontoxic Titanium(Iv)-Based Vacancy-Ordered Double Perovskite Halides with Tunable 1.0 to 1.8 Ev Bandgaps for Photovoltaic Applications. *ACS Energy Lett.* **2018**, *3*, 297–304.
- (30) Zhao, X.-G.; Yang, J.-H.; Fu, Y.; Yang, D.; Xu, Q.; Yu, L.; Wei, S.-H.; Zhang, L. Design of Lead-Free Inorganic Halide Perovskites for Solar Cells Via Cation-Transmutation. *J. Am. Chem. Soc.* **2017**, *139*, 2630–2638.
- (31) Zhao, X.-G.; Yang, D.; Sun, Y.; Li, T.; Zhang, L.; Yu, L.; Zunger, A. Cu—In Halide Perovskite Solar Absorbers. *J. Am. Chem. Soc.* 2017, 139, 6718–6725.
- (32) Xiao, Z.; Du, K.-Z.; Meng, W.; Wang, J.; Mitzi, D. B.; Yan, Y. Intrinsic Instability of $Cs_2In(I)M(III)X_6$ (M = Bi, Sb; X = Halogen) Double Perovskites: A Combined Density Functional Theory and Experimental Study. *J. Am. Chem. Soc.* **2017**, *139*, 6054–6057.
- (33) Xiao, Z.; Du, K.-Z.; Meng, W.; Mitzi, D. B.; Yan, Y. Chemical Origin of the Stability Difference between Cu (I)- and Ag (I)-Based Halide Double Perovskites. *Angew. Chem., Int. Ed.* **2017**, *56*, 12107–12111.
- (34) Slavney, A. H.; Leppert, L.; Bartesaghi, D.; Gold-Parker, A.; Toney, M. F.; Savenije, T. J.; Neaton, J. B.; Karunadasa, H. I. Defect-Induced Band-Edge Reconstruction of a Bismuth-Halide Double

- Perovskite for Visible-Light Absorption. J. Am. Chem. Soc. 2017, 139, 5015–5018.
- (35) Slavney, A. H.; Hu, T.; Lindenberg, A. M.; Karunadasa, H. I. A Bismuth-Halide Double Perovskite with Long Carrier Recombination Lifetime for Photovoltaic Applications. *J. Am. Chem. Soc.* **2016**, *138*, 2138–2141.
- (36) Filip, M. R.; Liu, X.; Miglio, A.; Hautier, G.; Giustino, F. Phase Diagrams and Stability of Lead-Free Halide Double Perovskites $Cs_2BB'X_6$: B = Sb and Bi, B' = Cu, Ag, and Au, and X = Cl, Br, and I. *J. Phys. Chem. C* **2017**, *122*, 158–170.
- (37) Filip, M. R.; Hillman, S.; Haghighirad, A. A.; Snaith, H. J.; Giustino, F. Band Gaps of the Lead-Free Halide Double Perovskites Cs₂BiAgCl₆ and Cs₂BiAgBr₆ from Theory and Experiment. *J. Phys. Chem. Lett.* **2016**, *7*, 2579–2585.
- (38) Du, K.-z.; Meng, W.; Wang, X.; Yan, Y.; Mitzi, D. B. Bandgap Engineering of Lead-Free Double Perovskite Cs₂ AgBiBr₆ through Trivalent Metal Alloying. *Angew. Chem., Int. Ed.* **2017**, *56*, 8158.
- (39) Dai, J.; Ma, L.; Ju, M.; Huang, J.; Zeng, X. C. In- and Ga-based inorganic double perovskites with direct bandgaps for photovoltaic applications. *Phys. Chem. Chem. Phys.* **2017**, *19*, 21691–21695.
- (40) Wei, F.; Deng, Z.; Sun, S.; Xie, F.; Kieslich, G.; Evans, D. M.; Carpenter, M. A.; Bristowe, P. D.; Cheetham, A. K. The synthesis, structure and electronic properties of a lead-free hybrid inorganic-organic double perovskite (MA)₂KBiCl₆ (MA = methylammonium). *Mater. Horiz.* **2016**, *3*, 328–332.
- (41) Tang, G.; Xiao, Z.; Hosono, H.; Kamiya, T.; Fang, D.; Hong, J. Layered Halide Double Perovskites $Cs_{3+n}M(II)_nSb_2X_{9+3n}$ (M = Sn, Ge) for Photovoltaic Applications. *J. Phys. Chem. Lett.* **2017**, *9*, 43–48
- (42) Deng, Z.; Wei, F.; Sun, S.; Kieslich, G.; Cheetham, A. K.; Bristowe, P. D. Exploring the Properties of Lead-Free Hybrid Double Perovskites Using a Combined Computational-Experimental Approach. J. Mater. Chem. A 2016, 4, 12025–12029.
- (43) McClure, E. T.; Ball, M. R.; Windl, W.; Woodward, P. M. Cs₂AgBiX₆ (X = Br, Cl): New Visible Light Absorbing, Lead-Free Halide Perovskite Semiconductors. *Chem. Mater.* **2016**, *28*, 1348–1354.
- (44) Volonakis, G.; Filip, M. R.; Haghighirad, A. A.; Sakai, N.; Wenger, B.; Snaith, H. J.; Giustino, F. Lead-Free Halide Double Perovskites Via Heterovalent Substitution of Noble Metals. *J. Phys. Chem. Lett.* **2016**, *7*, 1254–1259.
- (45) Chern, M. Y.; Vennos, D. A.; DiSalvo, F. J. Synthesis, structure, and properties of anti-perovskite nitrides Ca₃MN, M=P, As, Sb, Bi, Ge, Sn, and Pb. *J. Solid State Chem.* **1992**, *96*, 415–425.
- (46) Ovsyannikov, S. V.; Shchennikov, V. V. High-Pressure Routes in the Thermoelectricity or How One Can Improve a Performance of Thermoelectrics. *Chem. Mater.* **2010**, *22*, 635–647.
- (47) Kim, W. S.; Chi, E. O.; Kim, J. C.; Choi, H. S.; Hur, N. H. Close Correlation among Lattice, Spin, and Charge in the Manganese-Based Antiperovskite Material. *Solid State Commun.* **2001**, *119*, 507–510.
- (48) He, T.; Huang, Q.; Ramirez, A. P.; Wang, Y.; Regan, K. A.; Rogado, N.; Hayward, M. A.; Haas, M. K.; Slusky, J. S.; Inumara, K.; Zandbergen, H. W.; Ong, N. P.; Cava, R. J. Superconductivity in the Non-Oxide Perovskite MgCnI₃. *Nature* **2001**, *411*, 54–56.
- (49) Fang, H.; Jena, P. Li-Rich Antiperovskite Superionic Conductors Based on Cluster Ions. *Proc. Natl. Acad. Sci. U.S.A.* **2017**, *114*, 11046–11051.
- (50) Fang, H.; Wang, S.; Liu, J.; Sun, Q.; Jena, P. Superhalogen-Based Lithium Superionic Conductors. *J. Mater. Chem. A* **2017**, *5*, 13373–13381.
- (51) Barboni, D.; De Souza, R. A. The Thermodynamics and Kinetics of Iodine Vacancies in the Hybrid Perovskite Methylammonium Lead Iodide. *Energy Environ. Sci.* **2018**, *11*, 3266–3274.
- (52) Gebhardt, J.; Rappe, A. M. Transition Metal Inverse-Hybrid Perovskites. J. Mater. Chem. A 2018, 6, 14560–14565.
- (53) Gebhardt, J.; Rappe, A. M. Adding to the Perovskite Universe: Inverse-Hybrid Perovskites. ACS Energy Lett. 2017, 2, 2681–2685.

- (54) Bilal, M.; Ahmad, I.; Rahnamaye Aliabad, H. A.; Jalali Asadabadi, S. Detailed DFT studies of the band profiles and optical properties of antiperovskites SbNCa₃ and BiNCa₃. *Comput. Mater. Sci.* **2014**, *85*, 310–315.
- (55) Kresse, G.; Furthmüller, J. Efficient iterative schemes for ab initio total-energy calculations using a plane-wave basis set. *Phys. Rev. B: Condens. Matter Mater.* **1996**, 54, 11169.
- (56) Perdew, J. P.; Burke, K.; Ernzerhof, M. Generalized Gradient Approximation Made Simple. *Phys. Rev. Lett.* **1996**, *77*, 3865.
- (\$7) Heyd, J.; Scuseria, G. E.; Ernzerhof, M. Erratum: "Hybrid Functionals Based on a Screened Coulomb Potential" [J. Chem. Phys. 118, 8207 (2003)]. *J. Chem. Phys.* 2006, 124, 219906.
- (58) Freysoldt, C.; Grabowski, B.; Hickel, T.; Neugebauer, J.; Kresse, G.; Janotti, A.; Van de Walle, C. G. First-Principles Calculations for Point Defects in Solids. *Rev. Mod. Phys.* **2014**, *86*, 253
- (59) Gajdoš, M.; Hummer, K.; Kresse, G.; Furthmüller, J.; Bechstedt, F. Linear Optical Properties in the Projector-Augmented Wave Methodology. *Phys. Rev. B: Condens. Matter Mater. Phys.* **2006**, 73, 045112.
- (60) Yang, B.; Wang, L.; Han, J.; Zhou, Y.; Song, H.; Chen, S.; Zhong, J.; Lv, L.; Niu, D.; Tang, J. Cusbs2 as a Promising Earth-Abundant Photovoltaic Absorber Material: A Combined Theoretical and Experimental Study. *Chem. Mater.* **2014**, *26*, 3135–3143.
- (61) Chen, S.; Walsh, A.; Gong, X.-G.; Wei, S.-H. Classification of Lattice Defects in the Kesterite Cu₂ZnSnS₄ and Cu₂ZnSnSe₄ Earth-Abundant Solar Cell Absorbers. *Adv. Mater.* **2013**, *25*, 1522–1539.
- (62) Parrinello, M.; Rahman, A. Crystal Structure and Pair Potentials: A Molecular-Dynamics Study. *Phys. Rev. Lett.* **1980**, 45, 1196.
- (63) Allen, M. P.; Tildesley, D. J. Computer Simulation of Liquids; Oxford University Press, 2017.
- (64) Shi, Z.; Zhang, Z.; Kutana, A.; Yakobson, B. I. Predicting Two-Dimensional Silicon Carbide Monolayers. *ACS Nano* **2015**, *9*, 9802–9809.
- (65) Xu, S.-G.; Li, X.-T.; Zhao, Y.-J.; Liao, J.-H.; Xu, W.-P.; Yang, X.-B.; Xu, H. Two-Dimensional Semiconducting Boron Monolayers. *J. Am. Chem. Soc.* **2017**, *139*, 17233–17236.
- (66) Fonari, A.; Sutton, C. Effective Mass Calculator, 2012.
- (67) Yu, P. Y.; Cardona, M. Fundamentals of Semiconductors: Physics and Materials Properties; Springer, 1996.
- (68) Herz, L. M. Charge-Carrier Mobilities in Metal Halide Perovskites: Fundamental Mechanisms and Limits. *ACS Energy Lett.* **2017**, *2*, 1539–1548.
- (69) Walsh, A.; Zunger, A. Instilling Defect Tolerance in New Compounds. *Nat. Mater.* **2017**, *16*, 964.
- (70) Rühle, S. Tabulated values of the Shockley-Queisser limit for single junction solar cells. *Sol. Energy* **2016**, *130*, 139–147.
- (71) Shirayama, M.; Kadowaki, H.; Miyadera, T.; Sugita, T.; Tamakoshi, M.; Kato, M.; Fujiseki, T.; Murata, D.; Hara, S.; Murakami, T. N. Optical Transitions in Hybrid Perovskite Solar Cells: Ellipsometry, Density Functional Theory, and Quantum Efficiency Analyses for Ch₃Nh₃PbI₃. *Phys. Rev. Appl.* **2016**, *5*, 014012.